

Observation of exciton-phonon coupling in MoSe₂ monolayersS. Shree,¹ M. Semina,² C. Robert,¹ B. Han,¹ T. Amand,¹ A. Balocchi,¹ M. Manca,¹ E. Courtade,¹ X. Marie,¹ T. Taniguchi,³ K. Watanabe,³ M. M. Glazov,^{2,*} and B. Urbaszek^{1,†}¹*Université de Toulouse, INSA-CNRS-UPS, LPCNO, 135 Av. Rangueil, 31077 Toulouse, France*²*Ioffe Institute, 194021 St. Petersburg, Russia*³*National Institute for Materials Science, Tsukuba, Ibaraki 305-0044, Japan* (Received 17 April 2018; revised manuscript received 21 June 2018; published 16 July 2018)

We study experimentally and theoretically the exciton-phonon interaction in MoSe₂ monolayers encapsulated in hexagonal BN, which has an important impact on both optical absorption and emission processes. The exciton transition linewidth down to 1 meV at low temperatures makes it possible to observe high-energy tails in absorption and emission extending over several meV, not masked by inhomogeneous broadening. We develop an analytical theory of the exciton-phonon interaction accounting for the deformation potential induced by the longitudinal acoustic phonons, which plays an important role in exciton formation. The theory allows fitting absorption and emission spectra and permits estimating the deformation potential in MoSe₂ monolayers. We underline the reasons why exciton-phonon coupling is much stronger in two-dimensional transition metal dichalcogenides as compared to conventional quantum well structures. The importance of exciton-phonon interactions is further highlighted by the observation of a multitude of Raman features in the photoluminescence excitation experiments.

DOI: [10.1103/PhysRevB.98.035302](https://doi.org/10.1103/PhysRevB.98.035302)**I. INTRODUCTION**

Layered van der Waals materials provide a versatile platform for exploring fundamental physics and potential applications by combining different two-dimensional (2D) crystals [1–6]. Among these layered materials, transition metal dichalcogenides (TMDs) are particularly suitable for fundamental and applied optics, as they are semiconductors with a direct band gap when thinned down to one monolayer (ML) [3,4]. The Coulomb interaction between conduction electrons and valence holes is strong due to 2D confinement of charge carriers, heavy effective masses and weak screening. As a result, the optical properties of monolayer TMDs are dominated by excitons, electron-hole pairs bound by Coulomb attraction [7–14].

The interaction of excitons with phonons governs many important aspects of the optical properties of 2D materials [15–22] and semiconductor nanostructures in general [23–29] including energy relaxation, dephasing, and transition linewidth broadening with temperature. Under nonresonant optical excitation, high-energy excitons are generated that subsequently lose energy by phonon emission, as recently discussed for MoSe₂ MLs [30]. Interactions of carriers with phonons play a key role in the exciton formation process [31–34]. Other important signatures of the exciton-phonon interaction are single resonant and double resonant Raman scattering processes [35–40]. Also, the possible impact of polarons, electrons dressed by a phonon-cloud, on the optical properties has been discussed [41] for TMD MLs. There is a multitude of neutral and charged excitons in ML TMDs that

give rise to complex photoluminescence spectra [42]. Here phonons provide the necessary energy, and in certain cases momentum, for transitions between states in different valleys [43–45]. Knowing details about the interaction of excitons with phonons is therefore important for exciton dynamics that dominates light-matter interaction in TMD MLs.

The deformation potential is a key parameter which describes the interaction of the charge carriers and excitons with phonons. It controls a plethora of effects including momentum and energy relaxation processes, linewidth broadening, as well as the photoelastic properties of nanosystems relevant for optomechanical applications. The direct determination of the deformation potential, e.g., by shifts of the exciton line as a function of the elastic strain or deformation as in Refs. [46,47] is difficult due to the necessity of applying homogeneous uniaxial strain and requires substantial deformations in order to provide a measurable line shift. That is why the determination of the deformation potential values from other effects, like thermal broadening of the exciton emission lines and asymmetric shapes of the exciton absorption lines, is of high importance.

Recently, encapsulation in hexagonal boron nitride (hBN) of TMD monolayers has resulted in considerable narrowing of the exciton transition linewidth, down to about 1 meV [38,48–52]. This gives now access to interesting details of the exciton spectra. Here, we show in photoluminescence excitation spectroscopy on monolayer MoSe₂ encapsulated in hBN at $T = 4$ K a strong absorption tail at energies as high as 15 meV above the neutral exciton peak, well outside the transition linewidth. We demonstrate in resonant absorption experiments with a tunable laser that this high-energy tail is a very prominent feature in several samples investigated, underlining the importance of phonon-assisted exciton formation. In temperature-dependent PL experiments, we show a high-energy emission tail appearing as the temperature is

*glazov@coherent.ioffe.ru

†urbaszek@insa-toulouse.fr

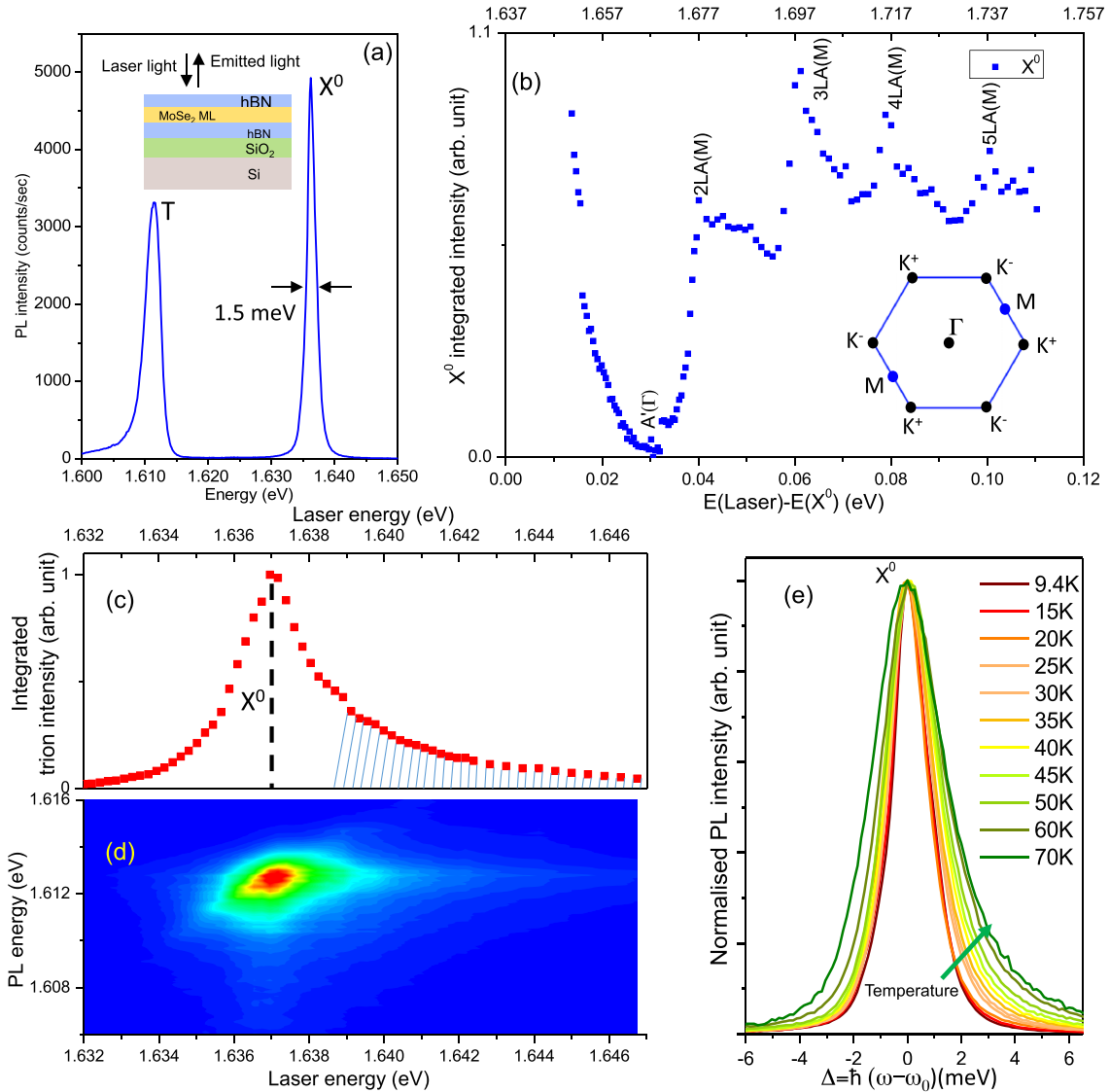


FIG. 1. Optical spectroscopy results. ML MoSe₂ encapsulated in hBN, *sample 1*, (a) typical PL emission spectrum at $T = 4$ K. Emission peaks at energy 1.613 and 1.637 eV are due to the charged (T) and the neutral exciton X^0 . [Inset of (a)] Schematics of sample structure: MoSe₂ ML encapsulated in hBN, the bottom hBN layer is (140 ± 5) nm thick as determined by AFM, the SiO₂ layer is 80 nm thick. (b) PLE experiments: integrated X^0 PL intensity plotted in terms of excess energy (bottom axis), defined as the difference between the laser energy (top axis) and the X^0 resonance. The average oscillation period corresponds to the M -point longitudinal acoustic phonon LA(M). [Inset of (b)] Schematics of 2D Brillouin zone with K , M , and Γ points (c) Integrated trion PL intensity as a function of excitation energy scanning laser across X^0 resonance and (d) contour plot of trion PL intensity scanning laser across X^0 resonance at $T = 4$ K. (e) Temperature dependent PL emission at X^0 resonance. For better comparison of emission shape, the X^0 PL intensity is normalized to the maximum value and the energy shifted to compensate the temperature evolution of the band gap.

raised from 9 to 70 K. We argue that the efficient interaction between exciton and acoustic phonons is responsible for both the broadening in absorption and the unusual evolution of the PL line with temperature observed on the same sample. Phonon sidebands in absorption spectra of ML MoSe₂ are discussed in Ref. [41]. Here, we provide evidence for this coupling at low temperature, previously masked by inhomogeneous broadening, and introduce exciton-acoustic phonon coupling as an important ingredient also for emission line-shape analysis. Based on model calculations within an analytical approach and taking into account the deformation potential interaction

between excitons and acoustic phonons, we obtain compact expressions for the absorption spectrum and phonon-assisted emission. This allows for a numerical fit of our absorption and emission experiments. We discuss the role of phonons in exciton formation and compare our findings to exciton-phonon interactions in quasi-2D quantum well structures.

The paper is organized as follows. In Sec. II, we report on experimental methods and results. Section III presents the model and analytical results. In Sec. IV, we compare the experiment and theory and estimate the exciton-acoustic phonon coupling strength. Conclusions are given in Sec. V.

II. OPTICAL SPECTROSCOPY RESULTS

A. Experimental methods

The samples are fabricated by mechanical exfoliation of bulk MoSe₂ (commercially available from 2D semiconductors) and very high-quality hBN crystals [53] on 80-nm-thick SiO₂ on a Si substrate. The experiments are carried out in a confocal microscope build in a vibration free, closed-cycle cryostat with variable temperature $T = 4\text{--}300$ K. The excitation/detection spot diameter is ~ 1 μm . The monolayer is excited by a continuous wave (cw) Ti-Sa laser (Msquared solstis) with sub- μeV linewidth. The photoluminescence (PL) signal is dispersed in a spectrometer and detected with a Si-CCD camera. The typical laser excitation power is 3 μW .

B. Experimental results

In PL experiments shown in Fig. 1(a), we observe well-separated (≈ 25 meV) emission lines for neutral (X^0 at ≈ 1.637 eV) and charged excitons (trions, T, at ≈ 1.613 eV) [54]. The transitions at low temperature in encapsulated MoSe₂ MLs show very narrow lines with a linewidth down to 1.2 meV [50]. This gives access to physical processes previously masked by inhomogeneous contributions to the linewidth. We study now in detail the quasisonant and resonant laser excitation of the X^0 transition. We start by discussing PL excitation (PLE) experiments detecting the X^0 PL emission intensity as a function of excitation laser energy. The integrated intensity of the X^0 transition is plotted in Fig. 1(b). We tune the laser from 1.651 to 1.747 eV in 2.5 meV steps (wavelength is incremented by $\Delta\lambda = 0.5$ nm). We observe oscillations of the PL intensity as a function of excitation energy, see also Figs. 2(a) and 2(c) for different samples. The period of the oscillation is ~ 20 meV and exactly matches the longitudinal acoustic phonon energy at the M point of the 2D hexagonal Brillouin zone, LA(M), as discussed in detail in Ref. [30]. As the excitation laser energy approaches the X^0 transition, we make an important observation; in Fig. 1(b), the PL emission intensity starts to increase considerably for excitation energies below 1.653 eV, even though the X^0 resonance is still ~ 15 meV away and the X^0 PL emission line is spectrally very narrow. We verified this surprising result by performing PLE measurements on different samples of MoSe₂ MLs encapsulated in hBN, compared in Fig. 2.

As we approach the X^0 transition with the laser, scattered laser light starts to obscure the PL signal on the CCD. In order to avoid this complication, we change detection scheme: we approach the X^0 resonance further with our laser but we detect the trion emission and assume that it is a reasonable measure of X^0 absorption. The excitation energy is tuned from 1.632 to 1.647 eV. The integrated trion emission intensity as a function of laser energy is recorded in Fig. 1(c). This X^0 absorption spectrum strongly deviates from a symmetric Lorentzian line shape, with a pronounced tail on the high-energy side of the main resonance. We have repeated this experiments for different laser powers and have reproduced each time this highly asymmetric line shape. Note that instead of monitoring the trion emission when scanning across the neutral exciton transition, also upconversion emission of the B-exciton and the excited A-exciton states can be monitored.

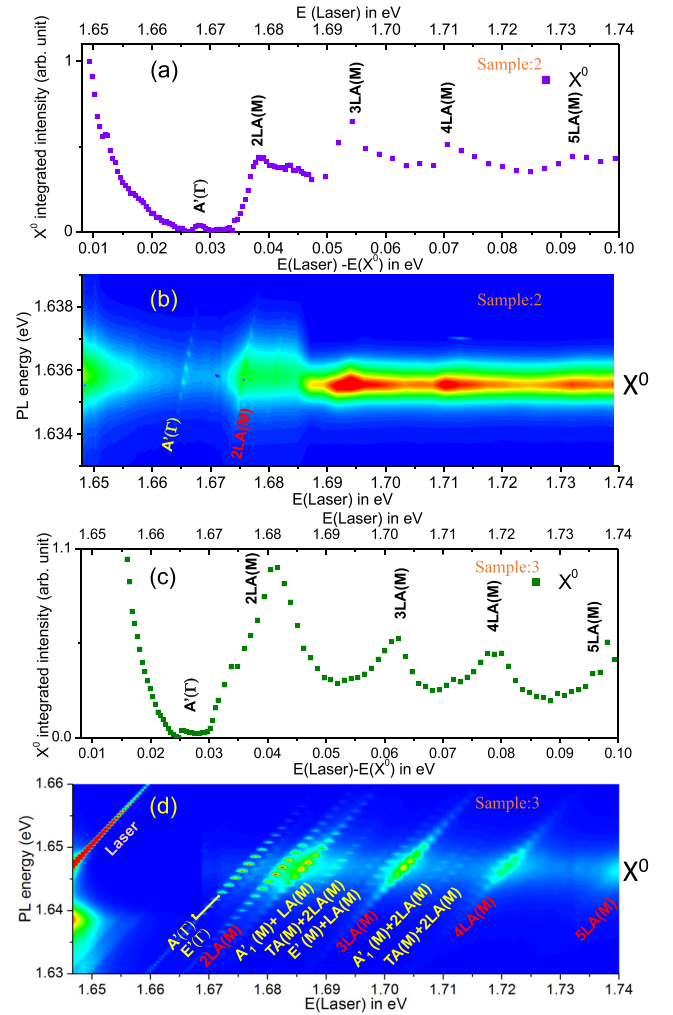


FIG. 2. Sample 2. (a) PLE spectra of MoSe₂ ML plotted in terms of excess energy (bottom axis), defined as the difference between the laser energy (top axis) and the X^0 resonance. (b) Contour plot of the same data, where sharp Raman features are superimposed on broad exciton absorption features. Sample 3. (c) Same as (a) but for different sample. (d) Same as (b) but for different sample. Phonons are labeled according to Soubelet *et al.* [40]. In samples with more disorder and stronger localization, Raman features are more prominent as momentum conservation is relaxed [40], which leads to rich features in (d). In addition to PL emission, the integrated signal in (a) and (c) also contains contributions from Raman scattered photons if the laser energy is a multiple of a prominent phonon energy above the X^0 transitions. In (b) and (d), the Raman features are spectrally very narrow due to the narrow linewidth of the excitation laser used.

These measurements further confirm the pronounced high-energy tail in absorption [55].

In addition to this high-energy tail in absorption, we also obtain a surprising result when studying emission at different temperature. In temperature-dependent PL from 10 to 70 K of the X^0 , shown in Fig. 1(d), we observe an asymmetric broadening, with stronger broadening on the high-energy side, a clear deviation from a standard Lorentzian emission line shape.

In the following section, we will explain the observed asymmetry in absorption and emission due to the efficient coupling of excitons to acoustic phonons. Especially the strong dependence on temperature of the asymmetry observed in emission is a strong indication that phonon related processes are important. Our theoretical investigation is further motivated by the efficient exciton-phonon coupling observed for two additional samples in Fig. 2. Also, for these samples, we confirm the strong absorption tail at higher energy, well above the X^0 resonance. In Figs. 2(a) and 2(c) for samples 2 and 3, respectively, this absorption tails are clearly observable up to 25 meV above the X^0 resonance. At higher excitation energy also for these samples we observe the multiphonon LA(M) resonances as for sample 1 in Fig. 1(b). In addition, samples 2 and 3 show strong resonant Raman signals, involving different phonons and their multiples, as indicated in Figs. 2(b) and 2(d).

III. THEORY OF EXCITON-PHONON INTERACTION

The aim of this section is to develop a simplified but analytical approach to exciton-phonon interaction in TMD monolayers. Here we argue that by taking into account the emission and absorption of acoustic phonons the broadening of the exciton line both in absorption at low temperature shown in Fig. 1(c) and in emission at higher temperature shown in Fig. 1(e) can be explained. We can fit the experiments to demonstrate order of magnitude agreement between our model and the measurements. For a complementary, self-consistent approach the reader is referred to Ref. [41], where a polaron framework was used and the link between dark (momentum-forbidden) excitons and phonon-side band formation is discussed in detail.

A. Deformation potential interaction

In semiconductors usually two types of interaction between excitons and acoustic phonons are discussed: the deformation potential interaction and the piezoelectric interaction [56,57]. Although the latter is typically dominant for individual charge carriers [56–58], the piezoelectric coupling is expected to be strongly suppressed for excitons in transition metal dichalcogenides due to the close values of effective masses of electrons and holes (predicted by theory [59]) and also due to the small exciton Bohr radius.

The deformation potential interaction involves, in the axially symmetric approximation, longitudinal acoustic phonons. This is because the energy shift of the charge carriers dispersion is, within the axial approximation, proportional to the divergence of the lattice displacements $\mathbf{u}(\mathbf{r})$: $\mathcal{U} \propto \nabla \cdot \mathbf{u}(\mathbf{r})$. Thus, $\mathcal{U} \neq 0$ for the longitudinal phonons only, where the displacements of atoms are parallel to the phonon wave vector. Hereafter, we consider only the phonons from the MoSe₂ monolayer because the electron-phonon deformation potential interaction occurs in general at short range. The van der Waals interaction between the monolayer and surrounding is relatively weak and, unlike ionic or covalent bonding, is not expected to efficiently transfer deformation from one layer to another. The exciton perturbation due to the deformation

potential reads

$$\mathcal{U}_q = \sqrt{\frac{\hbar}{2\rho\Omega_q S}} q b_q^\dagger (e^{-iqr_c} D_c - e^{-iqr_h} D_v) + \text{c.c.} \quad (1)$$

Here, \mathbf{q} is the phonon wave vector, b_q^\dagger (b_q) is the phonon creation (annihilation) operator, ρ is the two-dimensional density of mass of the TMD ML, $\Omega_q = sq$ is the phonon frequency, s is the (longitudinal) sound velocity, S is the normalization area, D_c (D_v) are the deformation potential constants for the conduction (valence) band, c.c. stands for the complex conjugate. The matrix element describing the exciton scattering from the state with the center of mass wave vector \mathbf{k} to the state with the center of mass wave vector \mathbf{k}' accompanied by the phonon emission is derived from Eq. (1) with the result

$$M_{\mathbf{k}'\mathbf{k}}^q = \sqrt{\frac{\hbar}{2\rho\Omega_q S}} q (D_c - D_v) \mathcal{F}(q) \delta_{\mathbf{k},\mathbf{k}'+\mathbf{q}}, \quad (2)$$

where the form factor

$$\mathcal{F}(q) = \int e^{-iq\rho/2} \varphi^2(\rho) d\rho = \frac{1}{[1 + (\frac{qa_B}{4})^2]^{3/2}}, \quad (3)$$

is introduced. Here and in what follows, we assume equal electron and hole effective masses, $\varphi(\rho) = \sqrt{2/(\pi a_B^2)} \exp(-\rho/a_B)$ is the ground-state envelope function (taken in the hydrogenic form), and a_B is the effective exciton Bohr radius. For relatively small phonon wave vectors $qa_B \ll 1$, the form factor is not sensitive to the shape of the envelope function.

B. Exciton-phonon scattering

In this section, we study the phonon-induced broadening of exciton resonance in the simplest possible approach based on the Fermi golden rule. To that end, we introduce the out-scattering rate from the exciton state with the wave vector \mathbf{k} and kinetic energy $E_k = \hbar^2 k^2 / 2M$, where M is the translational mass of the exciton, due to emission of the acoustic phonons:

$$\frac{1}{\tau_k} = \frac{2\pi}{\hbar} \sum_{\mathbf{k}'\mathbf{q}} |M_{\mathbf{k}'\mathbf{k}}^q|^2 \delta(E_k - E_{k'} - \hbar\Omega_q). \quad (4)$$

For $E_k, E_{k'} \gg E_s$, where $E_s = Ms^2$, the exciton-phonon scattering is quasielastic [56] (this point is discussed in detail below in Sec. III C), thus we can omit the phonon energy, $\hbar\Omega_q$, in the energy conservation δ function. Assuming that typical phonon and exciton wave vectors are smaller than the inverse Bohr radius, $k, k' \ll a_B^{-1}$ (this condition is fulfilled at all realistic temperatures), we put the form-factor $\mathcal{F} \equiv 1$ and obtain from Eq. (4),

$$\frac{1}{\tau_k} = 4 \frac{\sqrt{2E_s^3 E_k}}{\hbar \mathcal{E}}. \quad (5)$$

Here,

$$\mathcal{E}^{-1} = \frac{(D_c - D_v)^2}{4\pi \hbar^2 \rho s^4}. \quad (6)$$

Since exciton-phonon scattering is quasielastic, both absorption and emission processes are possible because the phonon energy $\hbar\Omega_q$ is typically much smaller than $k_B T$ with

TABLE I. Material parameters.

Property	MoSe ₂	MoS ₂	WSe ₂	WS ₂
s ($10^5 \times \text{cm/s}$) ^a	4.1	6.6	3.3	4.3
ρ ($10^{-7} \times \text{g/cm}^2$) ^b	4.46	3.11 ^c	6.04	4.32
c_1^{exper} ($\mu\text{eV/K}$)	91 ^d , 52...88 ^e	45, ^f 70 ^g	60 ^h	28 ^d
$ D_c - D_v ^{\text{fit}}$ (eV) ⁱ	5...6.5	5.5 ^f , 7.7 ^g , 10.5 ^j	5.4 ^k	3.5

^aFrom Ref. [62].

^bCalculated from the data on bulk crystals as $\rho = \rho_{\text{bulk}}c/2$, where c is the lattice constant for the 2H polytype.

^cFrom Ref. [63].

^dFrom Ref. [60].

^eThis work.

^fFrom Ref. [64].

^gFrom Ref. [50].

^hFrom Ref. [65].

ⁱFit to experimental data on c_1 (thermal broadening of exciton resonance) after Eq. (10).

^jFrom experimental data in Ref. [46] on strain tuning of optical resonances.

^kFrom experimental data in Ref. [47] on strain tuning of optical resonances.

T being the temperature and k_B the Boltzmann constant. Thus, for a thermalized exciton gas, one has

$$\frac{1}{\tau_T} = \frac{2\pi}{\hbar} \sum_{k'q} |M_{k'k}^q|^2 (1 + 2n_q) \delta(E_k - E_{k'}), \quad (7)$$

where

$$n_q = \frac{1}{\exp\left(\frac{\hbar\Omega_q}{k_B T}\right) - 1} \quad (8)$$

is the phonon occupation numbers. For $\hbar\Omega_q \ll E_k, E_{k'} \sim k_B T$, we have $n_q = k_B T / \hbar\Omega_q \gg 1$ and, as it follows from Eq. (7),¹

$$\frac{1}{\tau_T} = \frac{4\pi}{\hbar} \frac{E_s k_B T}{\mathcal{E}}. \quad (9)$$

The phonon-induced exciton linewidth can be roughly estimated making use of Eqs. (7) and (9) with the result

$$\frac{\hbar}{\tau_T} = c_1 T, \quad c_1 = 4\pi \frac{E_s k_B T}{\mathcal{E}}. \quad (10)$$

The parameter c_1 can be accessed in experiments [50,60,61], see also this work, Appendix A. Since the material parameters and the speed of sound are known to a large extent, the experimentally determined value of c_1^{exper} allows us to estimate the strength of the exciton-phonon interaction. Relevant parameters of exciton-phonon interaction are summarized in Table I. The analysis in Appendix A demonstrates that the accuracy of determination of c_1 parameter is not extremely high because at moderate to high temperatures the broadening can be dominated by the optical phonons and acoustic phonons at the Brillouin zone edge. Therefore the values c_1^{exper} and the

deduced deformation potentials can be considered as order-of-magnitude estimates only.

C. Phonon-assisted absorption and high-energy tail. Perturbative derivation

In this section, we aim to discuss exciton formation, assisted by phonons, for laser excitation energies below the first LA(M) resonance, i.e., closer than 19 meV to the neutral exciton resonance. In absence of exciton-phonon interaction, the absorbance of the transition metal dichalcogenide monolayer at the normal incidence of radiation in the spectral vicinity of exciton resonance is described by the Lorentzian profile

$$\mathcal{A}_0(\omega) = \frac{2\Gamma_0\Gamma}{(\hbar\omega - \hbar\omega_0)^2 + (\Gamma + \Gamma_0)^2}. \quad (11)$$

Here, ω is the incident light frequency, ω_0 is the exciton resonance frequency, Γ_0 is the exciton radiative decay rate, and Γ is the nonradiative decay rate of the exciton. This expression can be derived within the nonlocal dielectric response theory [66,67] by calculating the amplitude reflection $r(\omega)$ and transmission $t(\omega) = 1 + r(\omega)$ coefficients of the monolayer and evaluating the absorbance as $\mathcal{A}_0(\omega) = 1 - |r(\omega)|^2 - |t(\omega)|^2$. Hereafter, we disregard the effects related with the light propagation in the van der Waals heterostructure [68]. The estimates performed for our structures show that the asymmetry in the shape of the $\mathcal{A}_0(\omega)$ related to the light propagation effects is negligible.

To simplify derivations, in what follows, we consider in a first approach the limit of $\Gamma_0 \ll \Gamma$, which allows us to take into account the light-matter interaction perturbatively. In this limit, we can arrive at Eq. (11) making use of the Fermi's golden rule and evaluating the rate of the transitions to the excitonic state with the in-plane wave vector $\mathbf{k} = 0$ as

$$\mathcal{A}_0 = \frac{2\pi}{\hbar} |M_{\text{opt}}|^2 \delta(\hbar\omega - \hbar\omega_0). \quad (12)$$

Here, $|M_{\text{opt}}|^2$ is the squared matrix element of the optical transition to the $\mathbf{k} = 0$ state normalized per flux of the incident photons. The δ function ensuring the energy conservation is broadened by nonradiative processes

$$\delta(\hbar\omega - \hbar\omega_0) = \frac{1}{\pi} \frac{\Gamma}{(\hbar\omega - \hbar\omega_0)^2 + \Gamma^2}.$$

The radiative broadening of the exciton resonance can be introduced as $\Gamma_0 = |M_{\text{opt}}|^2 / \hbar$. Within second-order perturbation theory the phonon-assisted absorption [schematically shown in Fig. 3, panels (c) and (d)] is possible for $\hbar\omega > \hbar\omega_0$ via a two step process: First the exciton is created in the intermediate (virtual) state with $\mathbf{k} \simeq 0$ and the emission of the phonon takes place as a second step. Correspondingly, the contribution to absorbance due to this two-step process reads

$$\mathcal{A}_1 = \frac{2\pi}{\hbar} \sum_{k,q} \left| \frac{M_{k,0}^q M_{\text{opt}}}{\Delta} \right|^2 \delta(\Delta - E_k - \hbar\Omega_q). \quad (13)$$

Here,

$$\Delta = \hbar\omega - \hbar\omega_0 \quad (14)$$

is the detuning between the photon energy and the exciton resonance energy.

¹In Ref. [63] analogous expression, Eq. (25), was derived for the electron-phonon scattering.

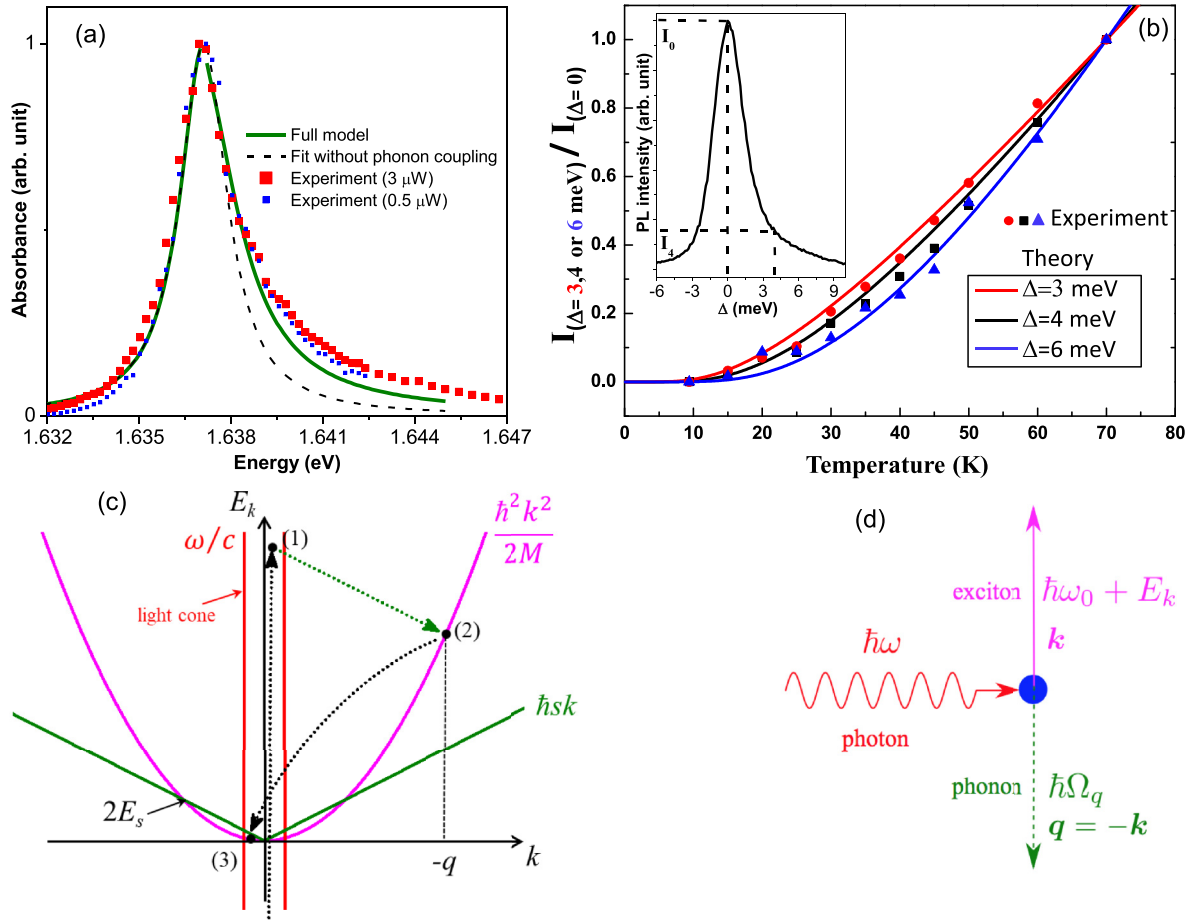


FIG. 3. (a) Absorbance at the A:1s exciton in MoSe₂ monolayer. Experimental data same as Fig. 1(c)—red squares, the data at a lower laser excitation power are shown as small blue squares, the full theory by a solid green curve, Eqs. (20) and (21), the black dashed curve shows the result in the absence of phonon-assisted transitions. $\Gamma_0 = \Gamma = 0.47$ meV, $|D_c - D_v| = 11$ eV, the other parameters are from Table I, in the calculation $T = 4$ K. (b) Normalized to the value at $T = 70$ K with the $T \rightarrow 0$ offset subtracted intensity of PL emission measured (symbols) and calculated after Eq. (24) (solid lines) as a function of temperature at a fixed detuning of $\Delta = 3$ (red), 4 (black), and 6 meV (blue). The parameters of the calculation are the same as in (a). (c) Schematics illustrating exciton and phonon dispersion, the intersection gives the energy scale $2Ms^2$, for $E_k \gg Ms^2$, the exciton-phonon interaction is quasielastic. Steps (1), (2), and (3) describe, respectively, photon absorption with exciton formation in a virtual state, exciton-phonon scattering resulting in a real final state for exciton (on the exciton dispersion, 2), and relaxation toward the radiative states inside the light cone (3). (d) Sketch of the photon absorption accompanied by the phonon emission. Exciton and phonon wave vectors have same absolute value but opposite directions.

It follows from the momentum conservation law that the phonon wave vector $\mathbf{q} = -\mathbf{k}$ as the total linear momentum of the electron-hole pair is equal to the in-plane photon momentum, which is close to zero at the normal incidence of radiation. The energy conservation law therefore reads

$$\frac{\hbar^2 k^2}{2M} + \hbar s k = \Delta. \quad (15)$$

Equation (15) can be readily solved to obtain the phonon energy in the form ($q = k$)

$$\hbar\Omega_k = E_s \left(\sqrt{1 + \frac{2\Delta}{E_s}} - 1 \right) \approx \begin{cases} \Delta, & \Delta \ll E_s, \\ \sqrt{2\Delta E_s}, & \Delta \gg E_s. \end{cases} \quad (16)$$

For typical parameters, $E_s \sim 100 \mu\text{eV} \ll \Delta$ and all energy is transferred to the recoil exciton, leaving the phonon with a

small energy $\sqrt{2\Delta E_s} \ll \Delta$. An illustration of the exciton and phonon dispersions is shown in Fig. 3(c). Summation over k in Eq. (13) can be performed for any ratio of Δ to E_s with the result

$$\mathcal{A}_1 = 2\pi\Gamma_0 \frac{\mathcal{F}^2(\Omega_k/s)}{\mathcal{E}} \mathcal{P}\left(\frac{\Delta}{E_s}\right) \Theta(\Delta), \quad (17)$$

where $\Theta(\Delta)$ is the Heaviside Θ function and the function $\mathcal{P}(x)$ is defined as

$$\mathcal{P}(x) = \frac{1}{\sqrt{1+2x}} \left(\frac{\sqrt{1+2x}-1}{x} \right)^2 \approx \begin{cases} 1, & x \ll 1, \\ \sqrt{2/x^3}, & x \gg 1. \end{cases} \quad (18)$$

For the experimentally relevant situation where $x = \Delta/E_s \gg 1$, the function $\mathcal{P}(x) \approx \sqrt{2}/x^{3/2}$ and \mathcal{A}_1 in Eq. (17) reduces to

$$\mathcal{A}_1 = 2\sqrt{2}\pi\Gamma_0 \frac{\mathcal{F}^2(\Omega_k/s)}{\mathcal{E}} \left(\frac{E_s}{\Delta}\right)^{3/2} \Theta(\Delta). \quad (19)$$

Expression (19) describes the tail of absorption at $\hbar\omega - \hbar\omega_0 \equiv \Delta \gg \Gamma, \Gamma_0, E_s$, and Ω_k is given by Eq. (16), similarly to what is predicted and observed in Ref. [41]. Accounting for both the phonon emission and absorption processes gives rise to an additional factor of $(1 + 2n_k)$ in Eq. (19).

For the purpose of direct comparison with experiment, it is convenient to obtain a model expression for the absorption spectrum, which accounts for both the (no-phonon) direct and indirect (phonon-assisted) processes. To that end, we employ the self-consistent Born approximation [69] for the exciton-phonon interaction, see Appendix B for details, and arrive at

$$\mathcal{A}(\hbar\omega) = \frac{2\Gamma_0[\Gamma + \gamma_{\text{ph}}(\Delta)]}{\Delta^2 + [\Gamma + \Gamma_0 + \gamma_{\text{ph}}(\Delta)]^2}, \quad (20)$$

where the acoustic phonon scattering rate is

$$\gamma_{\text{ph}}(\Delta) = \coth\left(\frac{\hbar\Omega_k}{2k_B T}\right) \frac{\pi \mathcal{F}^2(\Omega_k/s) \Delta^2}{\mathcal{E}} \mathcal{P}\left(\frac{\Delta}{E_s}\right) \Theta(\Delta). \quad (21)$$

In Eqs. (20) and (21), both phonon absorption and emission processes are included. Strictly speaking, the self-consistent Born approximation is not applicable for $\Delta \rightarrow 0$, because the smoothing of the Heaviside function should be also taken into account. The fully self-consistent approach such as developed in Ref. [41] should then be applied. In Eq. (20), the condition $\Gamma_0 \ll \Gamma$ is relaxed; that is why Γ_0 is present also in the denominator of Eq. (20). The results of calculation of $\mathcal{A}(\hbar\omega)$ are shown in Fig. 3(a) and fit very well the measured absorption spectra, they are discussed further in Sec. IV.

D. Temperature-dependent photoluminescence

In the photoluminescence process, the exciton formed nonresonantly relaxes in energy towards small k states. For a monolayer in free space, the light cone is defined as $q_{\text{phot}} = \omega/c$, c is the speed of light, and when $k(\omega) \leq q_{\text{phot}}$, the exciton can recombine by emitting a photon. In the absence of exciton-phonon interaction, the photoluminescence spectrum has a simple Lorentzian form, cf. Eq. (11). The exciton-phonon interaction makes states outside the light cone optically active as well. For example, an exciton with the wave vector \mathbf{k} can decay by emitting a phonon with wave vector $\mathbf{q} = \mathbf{k}$ and in addition a photon along the monolayer normal, i.e., $q_{\text{phot}} = 0$. For experiments at finite temperature, not only the phonon emission, but also phonon absorption processes become important.

In general, the calculation of the photoluminescence spectrum requires detailed analysis of the exciton energy relaxation and recombination processes [70,71]. Here, to simplify the consideration as we aim for a qualitative comparison with our experimental data, we assume that the excitons are thermalized and their occupation numbers are described by the Boltzmann

distribution

$$f_k = \exp\left(\frac{\mu - E_k}{k_B T}\right), \quad (22)$$

where $\mu < 0$ is the chemical potential of the exciton gas. The increase in temperature mainly results in occupation of higher energy excitonic states, which due to the quasi-elastic character of the exciton-phonon interaction gives rise to the high-energy wing in the photoluminescence, which is so striking for the experiments shown in Fig. 1(e). Denoting, as in Sec. III C, by $\hbar\omega$ the energy of the emitted photon, by $\hbar\omega_0$ the energy of the exciton at $k = 0$, and by Δ the detuning, Eq. (14), we arrive at the photon emission rate in the form [cf. (13)]

$$I(\omega) \propto \sum_{k,q} f_k (1 + 2n_q) \left| \frac{M_{0,k}^q M_{\text{opt}}}{\Delta} \right|^2 \delta(\Delta - E_k). \quad (23)$$

Equation (23) holds for $\Delta \gg \Gamma$, in the energy conservation δ function, the phonon energy is omitted. The calculation shows that the photoluminescence spectrum at the positive detunings related to the phonon-assisted emission takes the form

$$I(\omega) \propto e^{-\Delta/k_B T} \frac{k_B T E_s}{\Delta^2} \mathcal{F}^2\left(\frac{\sqrt{2\Delta E_s}}{\hbar s}\right), \quad \Delta \gg \Gamma. \quad (24)$$

The coefficient in Eq. (24) is temperature and detuning independent. For given detuning $\Delta > 0$, the relative photoluminescence intensity drastically increases with temperature mainly due to the presence of excitons with higher energies.

At the same time, the photoluminescence spectrum at $\omega < \omega_0$ (negative detuning $\Delta < 0$) is practically unaffected by the temperature increase. Indeed, to emit a photon with energy significantly (by more than $\hbar\Gamma$) lower than $\hbar\omega_0$, a phonon with the energy $\hbar\Omega_q \geq |\Delta|$ should be emitted as well. The rate of this process is given by

$$I(\omega) \propto \sum_{k,q} f_k (1 + n_q) \left| \frac{M_{0,k}^q M_{\text{opt}}}{\Delta} \right|^2 \delta(\Delta - E_k + \hbar\Omega_q). \quad (25)$$

Due to the energy conservation law, the process is allowed for small absolute values of detunings only, $|\Delta| \leq E_s/2$, see Fig. 3. Thus, for the experimentally relevant parameters, the photoluminescence increase at negative detunings is not expected in the theory, in agreement with the observation of an asymmetric line shape in Fig. 1(e). Note that this is somewhat different from the optical spectra in quantum dot structures where the exciton energy spectrum is discrete and exciton-phonon coupling is essentially inelastic. Thus, in quantum dots, deviations from Lorentzian line shapes with wings at low- and high-energy can appear [27,28].

IV. DISCUSSION

Figure 3(a) [same data as Fig. 1(c)] shows the X^0 absorption measured via the integrated trion PL intensity with a very prominent high energy tail. The results of our model calculations using Eqs. (20) and (21) for the best fit parameters (given in the caption) are shown by the red solid line. For comparison, the blue dashed curve shows the symmetric Lorentzian, which describes the low-energy wing of the absorption ($\hbar\omega < \hbar\omega_0$), but does not reproduce the high energy wing. In contrast, the

full calculation fits the spectrum and reproduces the observed absorption asymmetry very well, giving a strong indication that including exciton-phonon coupling is important for describing the absorption process.

The free parameters in our fit are the radiative, Γ_0 , and nonradiative, Γ damping of the exciton as well as the difference of the deformation potentials for the electron and hole, $|D_c - D_v|$. The value used for $\Gamma_0 = \Gamma \simeq 0.5$ meV is in order of magnitude agreement with results from time resolved spectroscopy reporting hundreds of femtoseconds to few picoseconds lifetimes [61,72,73]. The best fit value of $|D_c - D_v|$ of 11 eV is somewhat larger than the literature and experimental data summarized in Table I. The discrepancy can originate from the simplification of the model, particularly, the absence of the coupling with optical phonons as well as with phonons at the Brillouin zone edge, as well as from certain inaccuracy in determination of the deformation potentials, see Appendix A for a brief discussion of accuracy of fit of the temperature-induced broadening. Additionally, the presence of free charge carriers may also provide a contribution to the high-energy wing in absorption due to the possibility to relax the momentum conservation law. We also stress that the absorption [Figs. 1(c) and 3(a)] is detected via the photoluminescence of the trion, therefore, the efficiency of the relaxation pathway may play a role as well. Recent X^0 absorption experiments based on detecting upconversion PL have confirmed the high-energy absorption tail [55].

Similarly to the high energy tail in the absorption, the calculations predict the same asymmetry in the photoluminescence emission spectrum. As described in Sec. III D, this is because the excitons with wave vectors $k \gtrsim q_{\text{phot}} = \omega/c$ become optically active due to the phonon-assisted processes. The increase in the temperature gives rise to the increase of the occupancy of excitonic states at larger wave vectors. This is exactly what is observed in Fig. 1(e). Figure 3(b) shows the intensity of photoluminescence at three values of the positive detuning $\Delta = 3, 4, \text{ and } 6$ meV (all on the high-energy wing) as a function of temperature. The experimental data are in reasonable agreement with the calculation after Eq. (24) and indeed confirm the importance of the phonons in the photoluminescence emission.

Finally, we stress that the exciton interaction with acoustic phonons is particularly strong in TMD MLs and, generally, in two-dimensional crystals as compared with conventional quantum well structures such as GaAs/AlGaAs. This is because the density of states of two-dimensional phonons $\propto q$ is greatly enhanced compared to that of the bulk phonons $\propto q^2$. This results in about an order of magnitude enhancement (see Appendix C for details and further discussion) and accounts for the observation of the high-energy tails in exciton absorption in TMD monolayers.

V. CONCLUSION

Our combined experimental and theoretical study sheds light on the strong impact of the exciton-acoustic phonon interaction in TMD monolayers on exciton formation and recombination. We interpret the strong absorption above the exciton resonance in terms of phonon-assisted exciton formation. Asymmetric line shapes with high-energy tails in emission are observed in temperature dependent experiments. Also, this

unusual emission line shape is due to the deformation potential exciton-acoustic phonon coupling, which is enhanced in TMD monolayers as compared to conventional quantum well structures, and can be fitted by our simplified analytical theory.

ACKNOWLEDGMENTS

We are grateful to A. Knorr for discussions. We acknowledge funding from ANR 2D-vdW-Spin and ANR VallEx, ITN Spin-NANO Marie Skłodowska-Curie Grant Agreement No. 676108 and ITN 4PHOTON No. 721394, and Labex NEXT project VWspin. X.M. also acknowledges the Institut Universitaire de France. Growth of hexagonal boron nitride crystals was supported by the Elemental Strategy Initiative conducted by the MEXT, Japan and the CREST (JPMJCR15F3), JST. M.A.S. and M.M.G. acknowledge partial support from LIA ILNACS, RFBR projects 17-02-00383, 17-52-16020 and RF President Grant MD-1555.2017.2. M.A.S. acknowledges the partial support of the Government of the Russian Federation (Project No. 14.W03.31.0011 at the Ioffe Institute).

APPENDIX A: THERMAL BROADENING OF EXCITON LINE

Figure 4 presents the dependence of the exciton linewidth in photoluminescence (measured as full width at half maximum) on the sample temperature. Two fits are performed with very close values of parameters according to the general expression [60,64,74]

$$\gamma(T) \equiv \frac{\hbar}{\tau_T} = \gamma(0) + c_1 T + \frac{c_2}{\exp\left(\frac{\hbar\Omega_0}{k_B T}\right) - 1}. \quad (\text{A1})$$

Here, $\gamma(0)$ is the zero-temperature linewidth not related to the exciton-phonon interaction, the T -linear term is due to the

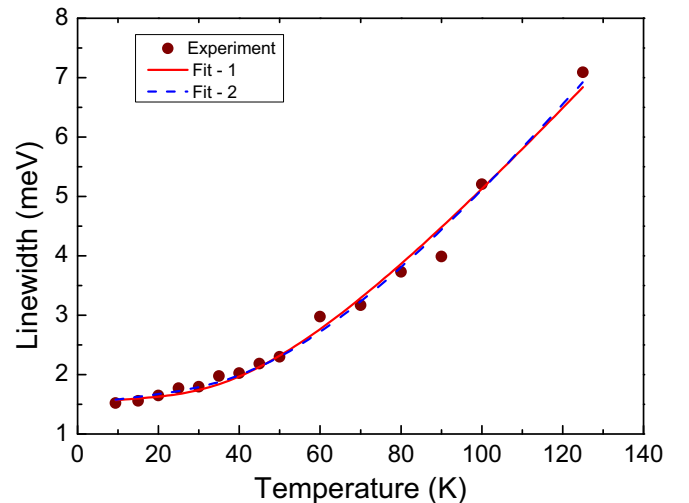


FIG. 4. Exciton linewidth ($2 \times$ half width at half maximum at the low-energy side) as a function of temperature extracted from the PL data in Fig. 1(c) (points). Fit 1 (red solid curve) is performed by Eq. (A1) with the parameter set $\gamma(0) = 1.52$ meV, $c_1 = 52$ $\mu\text{eV/K}$, $c_2 = 11.52$ meV, and $\hbar\Omega_0 = 13.4$ meV. Fit 2 (blue dashed curve) is performed by Eq. (A1) with the parameter set $\gamma(0) = 1.49$ meV, $c_1 = 88$ $\mu\text{eV/K}$, $c_2 = 14.9$ meV, and $\hbar\Omega_0 = 15.5$ meV.

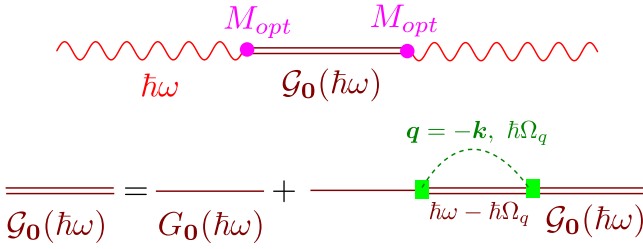


FIG. 5. Diagrams describing the photon absorption (top) and exciton dressed Greens function (bottom).

exciton-acoustic phonon scattering, Eq. (10), and the last term describes the interaction of excitons with optical phonons or acoustic phonons at the Brillouin zone edges, and $\hbar\Omega_0$ is the effective phonon energy. Reasonable fit quality can be achieved for the values of c_1 , which differ by a factor of 2 (compare fit-1 and fit-2 parameter sets in the figure caption).

APPENDIX B: NONPERTURBATIVE DERIVATION

For comparison with experiment, it is instructive to derive the expression for the indirect absorption spectrum relaxing the condition $\Delta \gg \Gamma$. To that end, we calculate the self-energy of the exciton with $\mathbf{k} = 0$ with account for the exciton-phonon interaction (allowing for, as before, the processes with the phonon emission only). In the self-consistent Born approximation, it takes the form (cf. Ref. [41] where similar expression has been derived by different method and see Fig. 5 for the diagrammatic representation)

$$\Sigma_0(\hbar\omega) = \sum_{\mathbf{k}, \mathbf{q}} |M_{\mathbf{k},0}^{\mathbf{q}}|^2 \mathcal{G}_{\mathbf{k}}(\hbar\omega - \hbar\Omega_{\mathbf{q}}), \quad (\text{B1})$$

where

$$\mathcal{G}_{\mathbf{k}}(\hbar\omega) = \frac{1}{\hbar\omega - \hbar\omega_0 - E_{\mathbf{k}} - \Sigma_{\mathbf{k}}(\hbar\omega)} \quad (\text{B2})$$

is the “dressed” and

$$G_{\mathbf{k}}(\hbar\omega) = \frac{1}{\hbar\omega - \hbar\omega_0 - E_{\mathbf{k}} + i\Gamma} \quad (\text{B3})$$

is the bare retarded Greens function of the exciton in the state \mathbf{k} . In derivation of Eqs. (B1) and (B2), we assumed that the photon damping is negligible and disregarded the diagrams with the self-crossings.² Furthermore, we assume that the phonon-induced renormalization of the (real) part of the exciton frequency, i.e., the polaron shift, are already included in ω_0 and $E_{\mathbf{k}}$ so that $\Sigma_{\mathbf{k}}(\hbar\omega)$ is purely imaginary. Note that self-consistent solution of Eqs. (B1) and (B2) is possible numerically only [41], it includes polaron effects as well. For $|\text{Im } \Sigma_{\mathbf{k}}(\hbar\omega)| \ll E_{\mathbf{k}}$, we obtain from Eqs. (B1) and (B2),

$$\begin{aligned} -\text{Im } \Sigma_0(\hbar\omega) &= \Gamma + \pi \sum_{\mathbf{k}, \mathbf{q}} |M_{\mathbf{k},0}^{\mathbf{q}}|^2 \delta(\hbar\omega - \hbar\omega_0 - \hbar\Omega_{\mathbf{q}}) \\ &= \Gamma + \gamma_{\text{ph}}(\Delta). \end{aligned} \quad (\text{B4})$$

²This is correct for not too small Δ where the final exciton state with the energy $E_{\mathbf{k}}$ is well-defined and the standard criteria of applicability of kinetic equation is fulfilled.

The phonon-induced contribution can be calculated similarly to the derivation of Eq. (17) with the result

$$\gamma_{\text{ph}}(\Delta) = \frac{\pi \mathcal{F}^2(\Omega_{\mathbf{k}}/s) \Delta^2}{\mathcal{E}} \mathcal{P}\left(\frac{\Delta}{E_s}\right) \Theta(\Delta). \quad (\text{B5})$$

With account for finite temperature effects (both emission and absorption) the contribution $\gamma_{\text{ph}}(\Delta)$ can be recast as

$$\begin{aligned} \gamma_{\text{ph}}(\Delta) &= (1 + 2n_q) \frac{\pi \mathcal{F}^2(\Omega_{\mathbf{k}}/s) \Delta^2}{\mathcal{E}} \mathcal{P}\left(\frac{\Delta}{E_s}\right) \Theta(\Delta) \\ &= \coth\left(\frac{\hbar\Omega_{\mathbf{k}}}{2k_B T}\right) \frac{\pi \mathcal{F}^2(\Omega_{\mathbf{k}}/s) \Delta^2}{\mathcal{E}} \mathcal{P}\left(\frac{\Delta}{E_s}\right) \Theta(\Delta), \end{aligned} \quad (\text{B6})$$

with $\hbar\Omega_{\mathbf{k}}$ given by Eq. (16).

The absorbance by the exciton is given by

$$\mathcal{A}(\hbar\omega) = -2\Gamma_0 \text{Im } \mathcal{G}_0(\hbar\omega) = \frac{2\Gamma_0[\Gamma + \gamma_{\text{ph}}(\Delta)]}{\Delta^2 + [\Gamma + \gamma_{\text{ph}}(\Delta)]^2}. \quad (\text{B7})$$

We also note that for arbitrary relation between Γ_0 and Γ , the radiative damping should be included only in the denominator of Eq. (B7), see Eq. (11) and Ref. [67]. At $\Delta \lesssim \Gamma$, the general expression (B7) passes to the direct absorbance, Eq. (11). At $\Delta \gg \Gamma$, Eq. (B7) provides the indirect transition contribution derived in Eq. (19). The photon self-energy is given by, up to a factor $\propto |M_{\text{opt}}|^2$, by the dressed exciton Greens function.

It is interesting to note that the approach developed above can be also applied for excitons interacting with free carriers or static disorder, if any. For example, for excitons interacting with short-range impurities, the $\gamma_{\text{ph}}(\Delta)$ in Eqs. (B4) and (B7) should be replaced by the Born scattering rate γ_{imp} (proportional to the impurity density and the electron-impurity scattering rate), which is independent on the exciton energy.

APPENDIX C: COMPARISON WITH CONVENTIONAL QUASI-TWO DIMENSIONAL SEMICONDUCTORS

The analysis shows that exciton-phonon interaction is quite strong in transition metal dichalcogenide MLs as compared with conventional GaAs-based quantum wells. For example, the parameter c_1 in GaAs quantum wells [74] is an order of magnitude smaller than in MoSe₂ despite higher values of deformation potential and the fact that excitons interact with bulk (3D) phonons in the GaAs case. Qualitatively, the enhanced exciton-phonon interaction in atom-thin crystals is due to the fact that for small wave vectors the phonon density of states is larger in 2D than in 3D. One can demonstrate this difference between TMD MLs and quantum well structures like GaAs/AlGaAs by determining the phonon scattering rate, as in Eq. (7), but in this case for two-dimensional excitons interacting with bulk (3D) phonons:

$$\frac{1}{\tau_T^{3D}} = \frac{2\pi}{\hbar} \sum_{\mathbf{k}', \mathbf{q}} |M_{\mathbf{k}'\mathbf{k}}^{3D:\mathbf{q}}|^2 (1 + 2n_q) \delta(E_{\mathbf{k}} - E_{\mathbf{k}'} - \hbar\Omega_{\mathbf{q}}). \quad (\text{C1})$$

Here,

$$M_{\mathbf{k}'\mathbf{k}}^{3D:\mathbf{q}} = \sqrt{\frac{\hbar}{2\rho_{\text{bulk}}\Omega_{\mathbf{q}}V}} q(D_c - D_v) \mathcal{F}(q_{\parallel}) \mathcal{F}_z(q_z) \delta_{\mathbf{k}, \mathbf{k}'+\mathbf{q}_{\parallel}}, \quad (\text{C2})$$

where ρ_{bulk} is the bulk mass density (gm/cm^3), V is the normalization volume, $\mathbf{q} = (\mathbf{q}_{\parallel}, q_z)$, and the form factor $\mathcal{F}_z(q_z)$ accounts for the exciton size quantization along the quantum well growth axis. In Eq. (C1) below, the sum over \mathbf{k}' is removed due to the momentum conservation law, $\mathbf{k}' = \mathbf{k} - \mathbf{q}$, while the sum over \mathbf{q} is transformed to the integral in the three-dimensional case as

$$\sum_{\mathbf{q}} = \frac{V}{(2\pi)^3} \int d\mathbf{q}_{\parallel} q_{\parallel} \int d\phi_{\mathbf{q}} \int dq_z,$$

where \mathbf{q}_{\parallel} is the in-plane wave vector of the phonon, $\phi_{\mathbf{q}}$ is the in-plane angle of the phonon wave vector, and q_z is its normal component. By contrast, in the case of excitons interacting with

two-dimensional phonons, the last integral over q_z is absent. As a result, for phonons with small energies $\hbar\Omega_{\mathbf{q}} \ll k_B T$, one has, instead of Eq. (7),

$$\frac{1}{\tau_T^{3D}} = \frac{(D_c - D_v)^2 M k_B T}{\hbar^2 \rho_{\text{bulk}} s^2} \int \mathcal{F}_z^2(q_z) \frac{dq_z}{2\pi} \sim \frac{1}{\tau_T} \times \frac{a_0}{a}, \quad (\text{C3})$$

where a_0 is the lattice constant and a is the well width (we took into account that $\int \mathcal{F}_z^2(q_z) dq_z / (2\pi) \sim 1/a$ and $\rho_{\text{bulk}} \sim \rho/a_0$). The parameter a_0/a is indeed small $\sim 0.1, \dots, 0.001$ for typical quantum well structures. Its appearance in Eq. (C1) as compared with Eq. (7) follows from a simple argument: for bulk phonons, the phonon density of states is $q^2 \rightarrow q_z q_{\parallel} \sim q_{\parallel}/a$.

-
- [1] K. S. Novoselov, A. Mishchenko, A. Carvalho, and A. H. Castro Neto, *Science* **353**, aac9439 (2016).
- [2] A. K. Geim and I. V. Grigorieva, *Nature (London)* **499**, 419 (2013).
- [3] K. F. Mak, C. Lee, J. Hone, J. Shan, and T. F. Heinz, *Phys. Rev. Lett.* **105**, 136805 (2010).
- [4] A. Splendiani, L. Sun, Y. Zhang, T. Li, J. Kim, C.-Y. Chim, G. Galli, and F. Wang, *Nano Lett.* **10**, 1271 (2010).
- [5] Q. H. Wang, K. Kalantar-Zadeh, A. Kis, J. N. Coleman, and M. S. Strano, *Nat. Nanotechnol.* **7**, 699 (2012).
- [6] K. F. Mak and J. Shan, *Nat. Photonics* **10**, 216 (2016).
- [7] G. Wang, A. Chernikov, M. M. Glazov, T. F. Heinz, X. Marie, T. Amand, and B. Urbaszek, *Rev. Mod. Phys.* **90**, 021001 (2018).
- [8] K. He, N. Kumar, L. Zhao, Z. Wang, K. F. Mak, H. Zhao, and J. Shan, *Phys. Rev. Lett.* **113**, 026803 (2014).
- [9] M. M. Ugeda, A. J. Bradley, S.-F. Shi, F. H. da Jornada, Y. Zhang, D. Y. Qiu, S.-K. Mo, Z. Hussain, Z.-X. Shen, F. Wang *et al.*, *Nat. Mater.* **13**, 1091 (2014).
- [10] A. Chernikov, T. C. Berkelbach, H. M. Hill, A. Rigosi, Y. Li, O. B. Aslan, D. R. Reichman, M. S. Hybertsen, and T. F. Heinz, *Phys. Rev. Lett.* **113**, 076802 (2014).
- [11] Z. Ye, T. Cao, K. O'Brien, H. Zhu, X. Yin, Y. Wang, S. G. Louie, and X. Zhang, *Nature (London)* **513**, 214 (2014).
- [12] D. Y. Qiu, F. H. da Jornada, and S. G. Louie, *Phys. Rev. Lett.* **111**, 216805 (2013).
- [13] A. Ramasubramaniam, *Phys. Rev. B* **86**, 115409 (2012).
- [14] G. Wang, X. Marie, I. Gerber, T. Amand, D. Lagarde, L. Bouet, M. Vidal, A. Balocchi, and B. Urbaszek, *Phys. Rev. Lett.* **114**, 097403 (2015).
- [15] X. Zhang, X.-F. Qiao, W. Shi, J.-B. Wu, D.-S. Jiang, and P.-H. Tan, *Chem. Soc. Rev.* **44**, 2757 (2015).
- [16] J. Ribeiro-Soares, R. M. Almeida, E. B. Barros, P. T. Araujo, M. S. Dresselhaus, L. G. Cancado, and A. Jorio, *Phys. Rev. B* **90**, 115438 (2014).
- [17] C. Rice, R. J. Young, R. Zan, U. Bangert, D. Wolverson, T. Georgiou, R. Jalil, and K. S. Novoselov, *Phys. Rev. B* **87**, 081307(R) (2013).
- [18] A. Molina-Sánchez and L. Wirtz, *Phys. Rev. B* **84**, 155413 (2011).
- [19] S. Horzum, H. Sahin, S. Cahangirov, P. Cudazzo, A. Rubio, T. Serin, and F. M. Peeters, *Phys. Rev. B* **87**, 125415 (2013).
- [20] T. Sekine, M. Izumi, T. Nakashizu, K. Uchinokura, and E. Matsuura, *J. Phys. Soc. Jpn.* **49**, 1069 (1980).
- [21] T. Jakubczyk, K. Nogajewski, M. R. Molas, M. Bartos, W. Langbein, M. Potemski, and J. Kasprzak, *2D Materials* **5**, 031007 (2018).
- [22] A. O. Slobodeniuk and D. M. Basko, *Phys. Rev. B* **94**, 205423 (2016).
- [23] S. Hameau, Y. Guldner, O. Verzelen, R. Ferreira, G. Bastard, J. Zeman, A. Lemaitre, and J. M. Gérard, *Phys. Rev. Lett.* **83**, 4152 (1999).
- [24] J. Lee, E. S. Koteles, and M. O. Vassell, *Phys. Rev. B* **33**, 5512 (1986).
- [25] M. C. Tatham, J. F. Ryan, and C. T. Foxon, *Phys. Rev. Lett.* **63**, 1637 (1989).
- [26] F. Gindele, U. Woggon, W. Langbein, J. M. Hvam, K. Leonardi, D. Hommel, and H. Selke, *Phys. Rev. B* **60**, 8773 (1999).
- [27] B. Urbaszek, E. J. McGhee, M. Krüger, R. J. Warburton, K. Karrai, T. Amand, B. D. Gerardot, P. M. Petroff, and J. M. Garcia, *Phys. Rev. B* **69**, 035304 (2004).
- [28] L. Besombes, K. Kheng, L. Marsal, and H. Mariette, *Phys. Rev. B* **63**, 155307 (2001).
- [29] P. Borri, W. Langbein, S. Schneider, U. Woggon, R. L. Sellin, D. Ouyang, and D. Bimberg, *Phys. Rev. Lett.* **87**, 157401 (2001).
- [30] C. M. Chow, H. Yu, A. M. Jones, J. R. Schaibley, M. Koehler, D. G. Mandrus, R. Merlin, W. Yao, and X. Xu, *npj 2D Mater Appl.* **1**, 33 (2017).
- [31] A. Bonnot, R. Planel, and C. B. à la Guillaume, *Phys. Rev. B* **9**, 690 (1974).
- [32] T. Amand, B. Dareys, B. Baylac, X. Marie, J. Barrau, M. Brousseau, D. J. Dunstan, and R. Planel, *Phys. Rev. B* **50**, 11624 (1994).
- [33] J. Szczytko, L. Kappei, J. Berney, F. Morier-Genoud, M. T. Portella-Oberli, and B. Deveaud, *Phys. Rev. Lett.* **93**, 137401 (2004).
- [34] A. Thilagam, *J. Appl. Phys.* **120**, 124306 (2016).
- [35] H. Guo, T. Yang, M. Yamamoto, L. Zhou, R. Ishikawa, K. Ueno, K. Tsukagoshi, Z. Zhang, M. S. Dresselhaus, and R. Saito, *Phys. Rev. B* **91**, 205415 (2015).
- [36] B. R. Carvalho, L. M. Malard, J. M. Alves, C. Fantini, and M. A. Pimenta, *Phys. Rev. Lett.* **114**, 136403 (2015).

- [37] G. Wang, M. M. Glazov, C. Robert, T. Amand, X. Marie, and B. Urbaszek, *Phys. Rev. Lett.* **115**, 117401 (2015).
- [38] C. M. Chow, H. Yu, A. M. Jones, J. Yan, D. G. Mandrus, T. Taniguchi, K. Watanabe, W. Yao, and X. Xu, *Nano Lett.* **17**, 1194 (2017).
- [39] M. R. Molas, K. Nogajewski, M. Potemski, and A. Babiński, *Sci. Rep.* **7**, 5036 (2017).
- [40] P. Soubelet, A. E. Bruchhausen, A. Fainstein, K. Nogajewski, and C. Faugeras, *Phys. Rev. B* **93**, 155407 (2016).
- [41] D. Christiansen, M. Selig, G. Berghäuser, R. Schmidt, I. Niehues, R. Schneider, A. Arora, S. M. de Vasconcelos, R. Bratschitsch, E. Malic *et al.*, *Phys. Rev. Lett.* **119**, 187402 (2017).
- [42] M. Koperski, M. R. Molas, A. Arora, K. Nogajewski, A. O. Slobodeniuk, C. Faugeras, and M. Potemski, *Nanophotonics* **6**, 1289 (2017).
- [43] H. Dery and Y. Song, *Phys. Rev. B* **92**, 125431 (2015).
- [44] H. Dery, *Phys. Rev. B* **94**, 075421 (2016).
- [45] J. Lindlau, C. Robert, V. Funk, J. Förste, M. Förg, L. Colombier, A. Neumann, E. Courtade, S. Shree, T. Taniguchi *et al.*, [arXiv:1710.00988](https://arxiv.org/abs/1710.00988).
- [46] G. Plechinger, A. Castellanos-Gomez, M. Buscema, H. S. J. van der Zant, G. A. Steele, A. Kuc, T. Heine, C. Schüller, and T. Korn, *2D Mater.* **2**, 015006 (2015).
- [47] R. Schmidt, I. Niehues, R. Schneider, M. Drüppel, T. Deilmann, M. Rohlfing, S. M. de Vasconcelos, A. Castellanos-Gomez, and R. Bratschitsch, *2D Mater.* **3**, 021011 (2016).
- [48] C. Jin, J. Kim, J. Suh, Z. Shi, B. Chen, X. Fan, M. Kam, K. Watanabe, T. Taniguchi, S. Tongay *et al.*, *Nat. Phys.* **13**, 127 (2017).
- [49] M. Manca, M. M. Glazov, C. Robert, F. Cadiz, T. Taniguchi, K. Watanabe, E. Courtade, T. Amand, P. Renucci, X. Marie *et al.*, *Nat. Commun.* **8**, 14927 (2017).
- [50] F. Cadiz, E. Courtade, C. Robert, G. Wang, Y. Shen, H. Cai, T. Taniguchi, K. Watanabe, H. Carrere, D. Lagarde *et al.*, *Phys. Rev. X* **7**, 021026 (2017).
- [51] O. A. Ajayi, J. V. Ardelean, G. D. Shepard, J. Wang, A. Antony, T. Taniguchi, K. Watanabe, T. F. Heinz, S. Strauf, X. Zhu *et al.*, *2D Mater.* **4**, 031011 (2017).
- [52] Z. Wang, J. Shan, and K. F. Mak, *Nat. Nanotechnol.* **12**, 144 (2017).
- [53] T. Taniguchi and K. Watanabe, *J. Cryst. Growth* **303**, 525 (2007).
- [54] Note that the peak commonly labeled trion can be due to indirect recombination processes (momentum dark excitons) [45]. In order to distinguish between the charged exciton and phonon-assisted recombination, reflectivity in the charge tunable structures can be used, cf. Ref. [75], which is beyond the scope of the present work on the neutral exciton.
- [55] B. Han, C. Robert, E. Courtade, M. Manca, S. Shree, T. Amand, P. Renucci, T. Taniguchi, K. Watanabe, X. Marie *et al.*, [arXiv:1805.04440](https://arxiv.org/abs/1805.04440).
- [56] V. Gantmakher and Y. Levinson, *Carrier Scattering in Metals and Semiconductors* (Elsevier, North-Holland, 1987).
- [57] Peter Y. Yu and Manuel Cardona, *Fundamentals of Semiconductors* (Springer-Verlag, Berlin, Germany, 2010), Chap. 7.
- [58] M. Danovich, I. L. Aleiner, N. D. Drummond, and V. I. Fal'ko, *IEEE J. Sel. Top. Quantum Electron.* **23**, 1 (2017).
- [59] X. Li, J. T. Mullen, Z. Jin, K. M. Borysenko, M. Buongiorno Nardelli, and K. W. Kim, *Phys. Rev. B* **87**, 115418 (2013).
- [60] M. Selig, G. Berghäuser, A. Raja, P. Nagler, C. Schüller, T. F. Heinz, T. Korn, A. Chernikov, E. Malic, and A. Knorr, *Nat. Commun.* **7**, 13279 (2016).
- [61] T. Jakubczyk, V. Delmonte, M. Koperski, K. Nogajewski, C. Faugeras, W. Langbein, M. Potemski, and J. Kasprzak, *Nano Lett.* **16**, 5333 (2016).
- [62] Z. Jin, X. Li, J. T. Mullen, and K. W. Kim, *Phys. Rev. B* **90**, 045422 (2014).
- [63] K. Kaasbjerg, K. S. Thygesen, and K. W. Jacobsen, *Phys. Rev. B* **85**, 115317 (2012).
- [64] P. Dey, J. Paul, Z. Wang, C. E. Stevens, C. Liu, A. H. Romero, J. Shan, D. J. Hilton, and D. Karaickaj, *Phys. Rev. Lett.* **116**, 127402 (2016).
- [65] G. Moody, C. K. Dass, K. Hao, C.-H. Chen, L.-J. Li, A. Singh, K. Tran, G. Clark, X. Xu, G. Berghäuser *et al.*, *Nat. Commun.* **6**, 8315 (2015).
- [66] M. M. Glazov, T. Amand, X. Marie, D. Lagarde, L. Bouet, and B. Urbaszek, *Phys. Rev. B* **89**, 201302 (2014).
- [67] E. L. Ivchenko, *Optical Spectroscopy of Semiconductor Nanostructures* (Alpha Science, Harrow UK, 2005).
- [68] C. Robert, M. A. Semina, F. Cadiz, M. Manca, E. Courtade, T. Taniguchi, K. Watanabe, H. Cai, S. Tongay, B. Lassagne *et al.*, *Phys. Rev. Mater.* **2**, 011001 (2018).
- [69] T. Ando and Y. Uemura, *J. Phys. Soc. Jpn.* **36**, 959 (1974).
- [70] L. I. Deych, M. V. Erementchouk, A. A. Lisyansky, E. L. Ivchenko, and M. M. Voronov, *Phys. Rev. B* **76**, 075350 (2007).
- [71] C. Piermarocchi, F. Tassone, V. Savona, A. Quattropani, and P. Schwendimann, *Phys. Rev. B* **53**, 15834 (1996).
- [72] C. Pöllmann, P. Steinleitner, U. Leierseder, P. Nagler, G. Plechinger, M. Porer, R. Bratschitsch, C. Schüller, T. Korn, and R. Huber, *Nat. Mater.* **14**, 889 (2015).
- [73] C. Robert, D. Lagarde, F. Cadiz, G. Wang, B. Lassagne, T. Amand, A. Balocchi, P. Renucci, S. Tongay, B. Urbaszek *et al.*, *Phys. Rev. B* **93**, 205423 (2016).
- [74] B. Jusserand, A. N. Poddubny, A. V. Poshakinskiy, A. Fainstein, and A. Lemaitre, *Phys. Rev. Lett.* **115**, 267402 (2015).
- [75] E. Courtade, M. Semina, M. Manca, M. M. Glazov, C. Robert, F. Cadiz, G. Wang, T. Taniguchi, K. Watanabe, M. Pierre *et al.*, *Phys. Rev. B* **96**, 085302 (2017).